

1 **Cryo-electron microscopy structure of a nucleosome-bound SWI/SNF chromatin**
2 **remodeling complex**

3

4 Yan Han¹, Alexis A Reyes^{1,2}, Sara Malik¹, Yuan He^{1,2,3,4,*}

5 1. Department of Molecular Biosciences, Northwestern University, Evanston, IL, USA

6 2. Interdisciplinary Biological Sciences Program, Northwestern University, Evanston,

7 USA

8 3. Chemistry of Life Processes Institute, Northwestern University, Evanston, IL, USA

9 4. Robert H. Lurie Comprehensive Cancer Center of Northwestern University,

10 Northwestern University, Chicago, USA

11

12 *Corresponding author (yuanhe@northwestern.edu)

13 **Abstract**

14 The multi-subunit chromatin remodeling complex SWI/SNF¹⁻³ is highly conserved from
15 yeast to humans and plays critical roles in various cellular processes including
16 transcription and DNA damage repair^{4,5}. It uses the energy from ATP hydrolysis to
17 remodel chromatin structure by sliding and evicting the histone octamer⁶⁻¹⁰, creating
18 DNA regions that become accessible to other essential protein complexes. However,
19 our mechanistic understanding of the chromatin remodeling activity is largely hindered
20 by the lack of a high-resolution structure of any complex from this family. Here we report
21 the first structure of SWI/SNF from the yeast *S. cerevisiae* bound to a nucleosome at
22 near atomic resolution determined by cryo-electron microscopy (cryo-EM). In the
23 structure, the Arp module is sandwiched between the ATPase and the Body module of
24 the complex, with the Snf2 HSA domain connecting all modules. The HSA domain also
25 extends into the Body and anchors at the opposite side of the complex. The Body
26 contains an assembly scaffold composed of conserved subunits Snf12
27 (SMARCD/BAF60), Snf5 (SMARCB1/BAF47/ INI1) and an asymmetric dimer of Swi3
28 (SMARCC/BAF155/170). Another conserved subunit Swi1 (ARID1/BAF250) folds into
29 an Armadillo (ARM) repeat domain that resides in the core of the SWI/SNF Body, acting
30 as a molecular hub. In addition to the interaction between Snf2 and the nucleosome, we
31 also observed interactions between the conserved Snf5 subunit and the histones at the
32 acidic patch, which could serve as an anchor point during active DNA translocation. Our
33 structure allows us to map and rationalize a subset of cancer-related mutations in the
34 human SWI/SNF complex and propose a model of how SWI/SNF recognizes and

- 35 remodels the +1 nucleosome to generate nucleosome-depleted regions during gene
36 activation¹¹⁻¹³.

37 **Main**

38 To gain insight into the molecular mechanisms of how SWI/SNF remodels chromatin,
39 we purified endogenous SWI/SNF from *S. cerevisiae*, assembled the SWI/SNF-
40 nucleosome complex *in vitro* (Extended Data Fig. 1) and determined its structure using
41 single particle cryo-EM. The complex was assembled in the presence of the non-
42 hydrolysable ATP analog ADP-BeF_x and was determined to sub-nanometer resolution
43 (Extended Data Fig. 2). We observed that the nucleosome is clamped between two
44 regions of the SWI/SNF complex (Fig. 1, Supplementary Video 1). To improve the
45 resolution, we also assembled the complex in the presence of ATPγS and determined
46 its structure using cryo-EM (Extended Data Fig. 3). Since this structure shows features
47 similar to the ADP-BeF_x bound complex, we combined the two data sets and performed
48 further processing (Extended Data Fig. 4). After careful 3D classification, we obtained a
49 reconstruction of the body of SWI/SNF to an average resolution of 4.7 Å (Fig. 1a;
50 Extended Data Fig. 4), which we refer to as the Body module of SWI/SNF. This
51 resolution allowed the *de novo* model building of the SWI/SNF complex (Fig. 1b).

52
53 In addition to the bound nucleosome, the SWI/SNF complex is composed of three major
54 modules: the Body, the Arp, and the ATPase (Fig. 2a). The Snf2 ATPase domain binds
55 the nucleosome at super helical location (SHL) 2, the same location shown in the stand-
56 alone structures of the Snf2 ATPase-nucleosome complexes^{14,15} as well as in SWR1¹⁶,
57 Chd1^{17,18} and SNF2h¹⁹, but quite different from INO80^{20,21} (Extended Data Fig. 5). The
58 Arp module is composed of Arp7, Arp9, Rtt102 and the HSA domain of Snf2 and is
59 sandwiched between the Body and the ATPase modules (Fig.1a, b). This architecture

60 has never been observed before and is quite different from other multi-subunit
61 remodeling complexes, including INO80 and SWR1^{16,20,21} (Extended Data Fig. 5). The
62 HSA of Snf2 plays an essential role in connecting the ATPase and Arp modules to the
63 Body, extending into the Body and anchoring at the opposite side of the complex (Fig.
64 1a, b). We therefore named this region of Snf2 adjacent to the HSA the Anchor domain
65 (Fig. 1c). This connection of the Arp module to the Body through a single α helix could
66 explain the observed flexibility of the Arp and ATPase modules in the reconstruction as
67 evidenced by lower estimated local resolution (Extended Data Figs. 2, 3). The functional
68 relevance of this flexibility requires further investigation.

69
70 The 4.7 Å resolution map of the Body shows the helical nature of the SWI/SNF (Fig. 1a)
71 and enabled us to build a structural model with the help of prior knowledge of this
72 important complex (Figs. 1b, 2; Methods). We then mapped the crosslinking data for
73 apo SWI/SNF²² onto our model of the Body module as a validation procedure (Extended
74 Data Table 1). Out of the 35 inter-linking pairs that were mapped onto the Body model,
75 27 (77%) pairs have a C α -C α distance within 30 Å, the maximum distance that is
76 allowed by using the crosslinker BS3²³. We also mapped 60 pairs of intra-links, of which
77 55 (92%) show a C α -C α distance within 30 Å. These comparisons demonstrate the
78 accuracy of our model, and also indicates that the structure of the SWI/SNF Body
79 module does not change drastically upon engaging a nucleosome.

80
81 The conserved subunits Swi1/ARID1/BAF250, Swi3/SMARCC/BAF150/177, Snf12/
82 SMARCD/BAF60 and Snf5/ SMARCB1/BAF47/INI1 assemble into the body of the

83 SWI/SNF complex (Fig. 2), consistent with these proteins forming a core module in the
84 human SWI/SNF complexes²⁴. Based on the positioning of different domains and their
85 functions, we further defined four sub-modules of the scaffold — the Spine, the Hinge,
86 the Arm and the Core (Fig. 2a).

87

88 The Spine is composed of Snf12 and the C-terminal regions of Swi3 (Fig. 2b). We
89 identified two copies (named A and B) of Swi3 in our structure, consistent with previous
90 crosslinking data showing multiple same-residue crosslinks within Swi3²². The most
91 striking feature of the Spine is the four-helix bundle formed by the two long helices
92 (LH1/2) of Snf12 and the Coiled-coil domains from two Swi3 (Fig. 2b), consistent with
93 previous finding that the RSC homologs of Snf12 (RSC6) and Swi3 (RSC8) directly
94 interact²⁵. The Coiled-coil domain of Swi3 has clear leucine-zipper properties,
95 containing hydrophobic amino acids separated by 7 residues in a helical region²⁶.

96 Interestingly, the crystal structure of the human dominant-negative OmoMYC
97 homodimer²⁷, a leucine-zipper containing complex, can be unambiguously fitted into the
98 two helices belonging to Swi3 by rigid body docking (Extended Data Fig. 6a).

99 Surprisingly, the two Coiled-coil domains of Swi3 have different lengths (Fig. 2b),
100 showing an asymmetric folding (Extended Data Fig. 6b). We speculate that this might
101 be due to the different interactions that the two Coiled-coils are involved in during
102 complex assembly. BAF155/170 (SMARCC1/2), the human homologues of Swi3, have
103 been indicated to form a dimer at the very first step of SWI/SNF complex assembly²⁴.

104 We therefore hypothesize that the two copies of Swi3 are indistinguishable at the early
105 steps of SWI/SNF assembly, and that after engaging with other subunits, especially

106 Snf12/SMARCD/BAF60, the symmetry is broken. Snf12 has been shown to play
107 important roles in SWI/SNF function²⁸, and our structure suggests that it may do so by
108 interacting with Swi3 and contributing to the assembly of the complex. The unassigned
109 density at the tip of the Spine shows clear β -sheet features and is directly connected to
110 the SWIB domain of Snf12 (Extended Data Fig. 6c). This, together with the secondary
111 structure prediction of Snf12, allowed us to assign this density to Snf12.

112

113 The Hinge is composed of the two SANT domains of Swi3 and the C-terminal helices of
114 Snf12 (Fig. 2c). SANT^B contacts the C-terminal helices of Snf12 and is in close
115 proximity to the Core sub-module (Fig. 2c), whereas SANT^A is located at the top and
116 interacts with a C-terminal segment of Swi3^A (Fig. 2c). Both SANT domains contact and
117 sandwich the Snf2 Anchor domain (Fig. 2c), playing a key role in stabilizing the ATPase
118 within the complex.

119

120 The Arm is composed of Snf5, the N-terminal SWIRM domains of Swi3 and C-terminus
121 of Swp82 (Fig. 2d). The Snf5 Core repeat (RPT) domains each engage one copy of the
122 Swi3 SWIRM domain in a similar manner as in the human BAF47/BAF155 crystal
123 structure²⁹ (Fig. 2d, Extended Data Fig. 7a, b). Subtle differences in the two RPT-
124 SWIRM interfaces (Extended Data Fig. 7c) are likely due to the α helix N-terminal to
125 RPT1, H-N, wedging between RPT1 and SWIRM^A while the C-terminal region of RPT2
126 is packed against the opposite side of SWIRM^B. The RPT1/SWIRM^A connects the Arm
127 module to the Core module by tightly associating with Swi1 (Fig. 2d). Swp82 contains
128 an α helix that runs along Snf5/Swi3 (Fig. 2d), likely further stabilizing the Arm module.

129 The environments that the two molecules of Swi3 experience in both the Hinge and the
130 Arm further establish the asymmetric architecture of this homodimer (Extended Data
131 Fig. 6b).

132

133 Swi1/ARID1/BAF250 resides in the core region of the Body, acting as a hub to integrate
134 all other modules (Fig. 2a, e). Therefore, we name it the Core module. It clearly folds
135 into an Armadillo (ARM) repeat structure³⁰ (Fig. 2e, Extended Data Fig. 8a).

136 Interestingly, BAF250a, the human homolog of Swi1, was predicted to contain an ARM
137 domain³¹, consistent with the highly conserved nature of this subunit. Compared to the
138 β -catenin structure³², the Swi1 ARM repeat domain contains extra insertion sequences
139 (Extended Data Fig. 8a), such as the one between helices H3 and H6. In addition to the
140 neighboring repeats, this long insertion makes extensive contacts with the Snf5 and
141 Swi3 subunits of the Arm as well as both the Spine and the Hinge. It contacts the Arm
142 by wrapping on top of the Swi3 SWIRM^A domain and traveling back along the Snf5 H-N
143 (Extended Data Fig. 8b). Interestingly, this insertion also forms an α helix H4 that
144 contacts a surface on SWIRM^B, whose corresponding region on SWIRM^A engages with
145 Swi1 H1 and Snf5 H-N (Extended Data Fig. 7d), emphasizing the role of Swi1 in
146 associating with the Arm module. In addition to this long insertion associating with the
147 Arm, H1 of Swi1 contacts the SWIRM^A domain of Swi3, whereas H3 and H8 interact
148 with Snf5 RPT1 (Extended Data Fig. 8b), thus connecting the Arm to the Core. The
149 Swi1 ARM repeat domain also interacts extensively with the Spine sub-module. The
150 entire top surface of the Swi1 ARM makes contacts with the helix bundle from the

151 Spine, with the C-terminal helices H19 and H20 engaging the SWIB domain of Snf12
152 (Extended Data Fig. 8c).

153

154 The Core is also the major docking point of the Snf2 Anchor domain (Fig. 3a). H11 of
155 Swi1 ARM interacts with an extended region of the Snf2 HSA domain that is absent
156 from the crystal structure³³, while H2, H6 and H9 contact the Anchor linker (Extended
157 Data Fig. 9a). These interactions, together with the Hinge region sandwiching the
158 Anchor helices of Snf2 (Extended Data Fig. 9b), further lock the ATPase in the complex.
159 This observation is consistent with ARID1A being the branching subunit connecting the
160 ATPase module with the rest of the SWI/SNF complex in humans²⁴.

161

162 The modular architecture of the SWI/SNF complex revealed by our structure agrees
163 well with the modules revealed by previous biochemical and proteomic studies^{34,35}. The
164 conserved SWI/SNF subunits form the structural scaffold within the complex, whereas
165 yeast-specific subunits only occupy peripheral regions. For example, Snf6 was identified
166 to situate at the back of the complex, spanning the Core and wrapping on top of the
167 four-helix bundle of the Spine (Extended Data Fig. 10a). Swp82 is another yeast-
168 specific subunit, and it is also located peripherally, making limited contacts with the rest
169 of the complex (Extended Data Fig. 10b). Based on our sequence conservation analysis
170 (Supplementary Figures 1-5), we have also mapped a subset of invariant residues from
171 the human cancer mutation database³⁶ onto our SWI/SNF model. Although the majority
172 of the mutations likely compromise structure and folding, many also map to protein-
173 protein interfaces, contributing to different types of the human disease (Fig. 2b-e, 3a).

174

175 Our structure has also enabled us to map the interactions between the SWI/SNF
176 complex and the nucleosome. The ATPase domain of Snf2 binds the nucleosome at
177 SHL2 in the context of the entire complex, as reported previously for the stand-alone
178 ATPase^{14,15,37,38}. A series of cancer patient mutations map to the Snf2 HSA-DNA
179 interface near SHL-6, likely diminishing the remodeling efficiency by disrupting protein-
180 DNA interactions (Fig. 3a). The yeast-specific subunit Swp82 also contacts the
181 nucleosomal DNA near SHL-2 (Fig. 3b), likely contributing to the remodeling activity of
182 SWI/SNF. Although the nucleosomal DNA is not deformed as was observed for
183 Chd1^{17,18}, there are multiple interactions between the SWI/SNF complex and the
184 extranucleosomal DNA in our structure. First, Snf6 contacts the extranucleosomal DNA
185 proximal to the nucleosome (Fig. 3b), in good agreement with previous site-directed
186 DNA crosslinking experiments³⁹. Second, at a lower threshold, we observed additional
187 density for extranucleosomal DNA contacting the Body module (Extended Data Fig. 11),
188 suggesting flexibility of this region of the DNA. However, when we prepared the
189 SWI/SNF-nucleosome complex using a nucleosome with no overhanging DNA
190 sequence (data not shown), we failed to observe stable complex formation, suggesting
191 the importance of the extranucleosomal DNA in nucleosome binding to SWI/SNF.
192 Interestingly, this extranucleosomal DNA also coincides with the possible trajectories of
193 the N-terminal regions of both Swi1 and Snf5 (Extended Data Fig. 11), which have been
194 shown to interact with acidic transcription activators⁴⁰⁻⁴². This could explain how
195 SWI/SNF is recruited by transcription activators to its target loci for chromatin
196 remodeling, leading to an activated gene transcription.

197

198 A connecting density is observed between the histones and Snf5 C-terminus (Fig. 3c,
199 d), consistent with the histone crosslinking experiments^{22,39}. This density likely
200 corresponds to the highly conserved Snf5 arginine anchor motif that interacts with the
201 acidic patch of the histone octamer (Fig. 3c, d) where a number of nucleosome
202 regulators bind⁴³, suggesting a conserved mechanism of octamer recognition. Deletion
203 of the RPT domains in Snf5 uncouples ATP hydrolysis by Snf2 with the chromatin
204 remodeling activity²². Our structure suggests an anchoring role of the Arm sub-module
205 during active remodeling, in which Snf5 locks the histones in place as the nucleosomal
206 DNA is being translocated, thus coupling ATP hydrolysis with chromatin remodeling
207 (Fig. 4). In contrast, this anchoring role is primarily carried out by the Arp module in
208 other large remodeling complexes, including INO80 and SWR1^{16,20,21} (Extended Data
209 Fig. 5). It has been well documented that the natural substrate for SWI/SNF is the +1
210 nucleosome situated near the promoter¹¹⁻¹³. Therefore, the extranucleosomal DNA at
211 the exit side of the nucleosome in our structure corresponds to upstream promoter
212 DNA, consistent with SWI/SNF's function in generating the nucleosome-depleted
213 regions during gene activation.

214 **Methods**

215 **SWI/SNF purification.**

216 SWI/SNF complex was purified from a yeast strain containing a TAP tag at the C-
217 terminus of Snf2⁴⁴ (obtained from the High Throughput Analysis Laboratory at
218 Northwestern University). Tandem affinity purification was performed as following. The
219 tagged yeast strain was grown to an optical density at 600nm (OD₆₀₀) of 4-5 in 12 liters
220 of YPD (3% glucose). Next, cells were harvested by centrifugation and washed with 200
221 ml of cold TAP Extraction Buffer (40 mM Tris pH 8, 250 mM ammonium sulfate, 1mM
222 EDTA, 10% glycerol, 0.1% Tween 20, 5 mM dithiothreitol [DTT], 2 mM
223 phenylmethylsulfonyl fluoride [PMSF], 0.31 mg/ml benzamidine, 0.3 µg/ml leupeptin, 1.4
224 µg/ml pepstatin, 2 µg/ml chymostatin). Cells were resuspended in 150 ml cold TAP
225 Extraction Buffer and lysed in a BeadBeater (Biospec Products). Cell debris was
226 removed by centrifugation at 14,000 ×g at 4°C for 1 hr. For the first affinity step, 2 ml
227 IgG Sepharose beads (GE Healthcare) were incubated with the lysate at 4°C overnight.
228 The beads were next washed and resuspended in 4 ml cold TEV (tobacco etch virus)
229 Cleavage Buffer (10 mM Tris pH8, 150 mM NaCl, 0.1% NP-40, 0.5 mM EDTA, 10%
230 glycerol). TEV cleavage using 25 µg of TEV protease was performed at room
231 temperature for 1 hr with gentle shaking. The TEV protease-cleaved products were
232 collected, and the IgG beads were washed with 3 column volumes (~6 ml total) cold
233 Calmodulin Binding Buffer (15 mM HEPES pH7.6, 1 mM magnesium acetate, 1 mM
234 imidazole, 2 mM CaCl₂, 0.1% NP-40, 10% glycerol, 200 mM ammonium sulfate, 5 mM
235 DTT, 2 mM PMSF, 0.31 mg/ml benzamidine, 0.3 µg/ml leupeptin, 1.4 µg/ml pepstatin, 2
236 µg/ml chymostatin). CaCl₂ was added to the combined eluate at a final concentration of

237 2 mM and incubated with 0.8 ml Calmodulin Affinity Resin (Agilent Technologies) at 4°C
238 for 2 hours. After incubation, the beads were washed with cold Calmodulin Binding
239 Buffer and cold Calmodulin Wash Buffer (same as Calmodulin Binding Buffer, but
240 containing 0.01% NP-40), and bound proteins were eluted with Calmodulin Elution
241 Buffer (15 mM HEPES pH 7.6, 1 mM magnesium acetate, 1 mM imidazole, 2 mM
242 EGTA, 10% glycerol, 0.01% NP-40, 200 mM ammonium sulfate) at room temperature.
243 Fractions containing the SWI/SNF complex were combined and concentrated to a final
244 concentration of ~4 mg/ml (280 nm absorption) using a concentrator (Amicon Ultra-4
245 Ultracel 30K, Millipore). Concentrated protein was aliquoted, flash frozen in liquid
246 nitrogen and stored at -80°C.

247

248 **Nucleosome reconstitution.**

249 Mono-nucleosome was reconstituted with *Xenopus* histones and the 601 DNA⁴⁵ using
250 the Mini Prep Cell (Bio-rad) as described previously⁴⁶. The *Xenopus* histones were
251 obtained from the Histone Source – the Protein Expression and Purification (PEP)
252 Facility at Colorado State University. DNA oligonucleotides containing the 601
253 sequence were purchased from IDT (Integrated DNA Technology): top strand, 5'-
254 ACCTCCCACTATTTTATGCGCCGGTATTGAACCACGCTTATGCCAGCATCGTTAA
255 TCGATGTATATATCTGACACGTGCCTGGAGACTAGGGAGTAATCCCCTTGGCGGT
256 AAAACGCGGGGACAGCGCGTACGTGCGTTTAAGCGGTGCTAGAGCTGTCTACG
257 ACCAATTGAGCGGCCTCGGCACCGGGATTCTGAT-3'; bottom strand, 5'-
258 ATCAGAATCCCGGTGCCGAGGCCGCTCAATTGGTCGTAGACAGCTCTAGCACCGC
259 TTAAACGCACGTACGCGCTGTCCCCGCGTTTTAACCGCCAAGGGGATTACTCCC

260 TAGTCTCCAGGCACGTGTCAGATATATACATCGATTAACGATGCTGGGCATAAGCG
261 TGGTTCAATACCGGCAT-3'. The 601 sequence is underlined. The lyophilized DNA
262 oligos were resuspended in water to a final concentration of ~100 μ M and mixed at 1:1
263 molar ratio. Annealing of the DNA was performed by incubating in boiling water for 5
264 min followed by gradually cooling to room temperature in 2 hours. The reconstituted
265 nucleosome core particle (NCP) was concentrated to ~6 μ M and annealed with a
266 biotinylated RNA molecule (IDT, 5'-UAGUGGGAGGU-3'-biotin) to the top DNA strand at
267 1:1.5 (DNA to RNA) molar ratio at 45°C for 5 min followed by gradually cooling to room
268 temperature in 30-40 min. This resulted in a final concentration of the nucleosome core
269 particle (NCP) at 5.52 μ M. The annealed NCP was stored at 4°C.

270

271 **SWI/SNF-NCP assembly.**

272 To assemble the SWI/SNF-NCP complex, we modified our approach of reconstituting
273 Pol I/II/III pre-initiation complexes (PIC)⁴⁷⁻⁴⁹ and used the NCP to replace the nucleic
274 acid scaffold. Specifically, 0.4 μ l of the biotin-RNA-annealed NCP (0.552 μ M, 1/10 of the
275 storage concentration) was first mixed with 1 μ l of the assembly buffer (12 mM HEPES
276 pH 7.9, 0.12 mM EDTA, 12% glycerol, 8.25 mM MgCl₂, 1 mM DTT, 2 mM ADP, 32mM
277 KF, 4mM BeCl₂ and 0.05% NP-40 [Roche]). Next, 1 μ l of the concentrated SWI/SNF
278 complex was added to this mixture and incubated at room temperature for 2 hours.
279 Assembled complex was immobilized onto the magnetic streptavidin T1 beads
280 (Invitrogen) which had been equilibrated with the assembly buffer plus 60 mM KCl and
281 minus ADP-BeF_x. Following washing of the beads two times using a wash buffer (10
282 mM HEPES, 10 mM Tris, pH 7.9, 5% glycerol, 5 mM MgCl₂, 50 mM KCl, 1 mM DTT,

283 0.05% NP-40, 1 mM ADP, 16mM KF, 2mM BeCl₂), the complex was eluted by
284 incubating the beads at room temperature for 30 min with 3μl digestion buffer containing
285 10 mM HEPES, pH 7.9, 10 mM MgCl₂, 50 mM KCl, 1 mM DTT, 5% glycerol, 0.05% NP-
286 40, 1 mM ADP, 16mM KF, 2mM BeCl₂ and 0.05 unit/μl RNase H (New England
287 Biolabs). The SWI/SNF-NCP complex assembled in the presence of ATP_γS was
288 performed essentially as described above with 1mM (2mM in the first assembly buffer)
289 ATP_γS replacing ADP-BeF_x in the buffers.

290

291 **Electron microscopy.**

292 The assembled SWI/SNF-NCP complex was first crosslinked using 0.05%
293 glutaraldehyde under very low illumination conditions on ice for 5 min before applied
294 onto EM grids. Negative staining sample preparation and data collection were
295 performed as previously described⁴⁸. For cryo sample preparation, crosslinked complex
296 (~3.3 μl) was applied onto a 400 mesh Quantifoil grid containing 3.5 μm holes and 1 μm
297 spacing (Quantifoil 3.5/1, Electron Microscopy Sciences). A thin carbon film was floated
298 onto the grid before it was plasma cleaned for 10s at 5 W power using a Solarus plasma
299 cleaner (Gatan) equipped with air immediately before sample deposition. The sample
300 was allowed to absorb to the grid for 10 min at 4°C and 100% humidity in a Vitrobot
301 (FEI) under low illumination conditions, before blotted for 4 s at 10 force and plunge-
302 frozen in liquid ethane. The frozen grids were stored in liquid nitrogen until imaging.

303

304 Cryo-EM data collection was performed using a JEOL 3200FS transmission electron
305 microscope (JEOL) equipped with a K2 Summit direct electron detector (Gatan)

306 operating at 200kV (Extended Data Table 2). Data were collected using the K2 camera
307 in counting mode at a nominal magnification of 30,000 × (1.12 Å per pixel). Movie series
308 with defocus values ranging from -1.5 to -4.5 μm were collected using Legikon⁵⁰. 40-
309 frame exposures were taken at 0.3 s per frame (12 s total), using a dose rate of 8 e⁻ per
310 pixel per second, corresponding to a total dose of 76.5 e⁻ Å⁻² per movie series. Four
311 datasets with a total number of 7,769 movies on the ADP-BeF_x sample and four other
312 datasets with a total number of 6,903 movies on the ATPγS sample were collected.

313

314 **Image processing and three-dimensional reconstruction.**

315 Negative stain data pre-processing was performed using the Appion processing
316 environment⁵¹. Particles were automatically selected from the micrographs using a
317 difference of Gaussians (DoG) particle picker⁵². The contrast transfer function (CTF) of
318 each micrograph was estimated using CTFFind4⁵³, the phases were flipped using
319 CTFFind4, and particle stacks were extracted using a box size of 128 × 128 pixels.
320 Two-dimensional classification was conducted using iterative multivariate statistical
321 analysis and multi-reference alignment analysis (MSA-MRA) within the IMAGIC
322 software⁵⁴. Three-dimensional (3D) reconstruction of negative stained data was
323 performed using an iterative multi-reference projection-matching approach containing
324 libraries from the EMAN2 software package⁵⁵. The initial 3D model was generated using
325 cryoSPARC⁵⁶.

326

327 Cryo-EM data was pre-processed as follows. Movie frames were aligned using
328 MotionCor2⁵⁷ to correct for specimen motion. Particles were automatically selected from

329 the aligned and dose-weighted micrographs using Gautomatch (developed by Zhang K,
330 MRC Laboratory of Molecular Biology, Cambridge, UK) with 2-fold binning
331 (corresponding to 2.24Å/pixel). The CTF of each micrograph and of each particle was
332 estimated using Gctf⁵⁸. All three-dimensional (3D) classification and refinement steps
333 together with postprocess and local resolution estimation were performed within
334 RELION 3.0⁵⁹.

335
336 For the ADP-BeF_x dataset, 891,573 particles were automatically picked and were
337 subjected to an initial round of 3D classification with alignment using the density
338 obtained from negative staining as the initial reference (Extended Data Fig. 2). The
339 “Angular sampling interval”, “Offset search range (pix)” and “Offset search step (pix)”
340 were set to 15 degrees, 10 and 2, respectively, for the first 50 iterations. Next, these
341 values were set back to default (7.5 degrees, 5, 1) and the 3D classification was
342 continued until convergence. This resulted in class 3 with 198,543 particles showing
343 sharp structural features of SWI/SNF and nucleosome. This class was subsequently
344 refined and further classified without alignment into 5 classes with a mask around the
345 Arp module and the nucleosome (Extended Data Fig. 2b). Class 1 with 35,214 particles
346 from this second round of classification showed best features of the nucleosome and
347 was chosen to proceed with 3D auto-refinement, which yielded a structure of SWI/SNF-
348 NCP at an overall resolution of 8.96Å (Extended Data Fig. 2c). All resolutions reported
349 herein correspond to the gold-standard Fourier shell correlation (FSC) using the 0.143
350 criterion⁶⁰. The ATP γ S dataset with 820,117 particles was processed in a similar
351 manner (Extended Data Fig. 3), resulting in a structure with an overall resolution of 10Å.

352

353 To focus on the Body of SWI/SNF, we combined the particles from both samples after
354 the first round of 3D classification with a total number of 390,573 particles (Extended
355 Data Fig. 4). Next, signal subtraction on the nucleosome and the lower half of the Arp
356 module was performed as previously described⁶¹, leaving the SWI/SNF Body module
357 and the top half of the Arp module intact. Subsequently, a 3D classification was
358 performed with only local alignment turned on. This resulted in class 5 with 61,518
359 particles showing the best structural features of the Body module (Extended Data Fig.
360 4b). Next, we unbinned and refined the original particle stack of this class, and
361 generated masks around the Body module, the Arp module plus the ATPase density of
362 Snf2, and the nucleosome (Extended Data Fig. 4b). 3D multi-body refinement⁶² was
363 then performed on this class, which drastically improved the resolution of the Body
364 module to 4.7Å (Extended Data Fig. 4c). The core region of the Body module has a
365 resolution close to 4.3Å (Extended Data Fig. 4b), showing densities of bulky sidechains,
366 which enabled us to partially build the structural model of the Body module (Fig. 1b).
367 This body map replaced its corresponding region in the ADP-BeF_x map to result in the
368 composite map shown in Fig. 1a.

369

370 **Model building.**

371 To aid in model building, we performed secondary structure prediction of the SWI/SNF
372 subunits using the Genesilico Metaserver⁶³. Sequence alignment of the conserved
373 SWI/SNF subunits were performed using CLC Sequence Viewer 7 (Supplementary
374 Figures 1-5). To build the structural model of the SWI/SNF Body module, we first

375 performed rigid body docking of known structures into our 4.7Å Body map. The rigid-
376 body docking was performed in UCSF Chimera^{64,65}, which yielded good fit of the
377 following structures: the SNF5 Repeat domains (RPTs) and Swi3 SWIRM domains from
378 the human BAF47/BAF155 complex (PDB ID 5GJK)²⁹, the SANT domain of the yeast
379 Swi3 (PDB ID 2YUS), and the SWIB domain of mouse BAF60a (PDB ID 1UHR). The
380 BAF47/BAF155 heterodimer and the Swi3 SANT domain can be docked in the density
381 map at two distinct locations, indicating two copies of these domains. Indeed, chemical
382 crosslinking combined with mass spectrometry has shown at least two copies of Swi3 in
383 the yeast SWI/SNF complex²², confirming our docking experiment. Yeast Snf5 has been
384 annotated with two SNF5 RPT domains in Pfam (<http://pfam.xfam.org/protein/P18480>).
385 We observed clear density in our map that connects these two RPT domains. Next, we
386 built homology models of these structures using Modeller⁶⁶ and replaced the docked
387 PDBs in the Body density map. Regions with missing or extra connecting density were
388 then manually deleted or built in Coot⁶⁷ based also on secondary structure predictions
389 of these proteins.

390
391 The Snf2 Anchor domain was built manually in Coot. First, the Arp7/Arp9/Rtt102/HSA
392 structure (PDB ID 4I6M)³³ was rigid body docked into the full map, which helped in
393 registering the HSA helix in the Body map. The HSA helix was then manually extended
394 in Coot, with Y586 matching a sidechain density further confirming the register of this
395 helix. Next, the Anchor domain was manually extended from the end of the HSA by
396 following the connected density of the map. Again, secondary structure prediction was

397 also used as a guide when extending the model in Coot. Bulky sidechain density at
398 Y497, Y533 and W554 further confirmed the model.
399
400 The ARM repeat domain of Swi1 locates in the core region of the Body map with the
401 highest local resolution, therefore enabling *de novo* model building. First, the helix
402 density corresponding to residues 942-955 of Swi1 was chosen to model because it has
403 the highest local resolution and that it contains a few bulky sidechain densities. Next,
404 two α helices with poly-alanine sequence were generated in Coot, which allowed us to
405 create a bulky residue (lysine, arginine, histidine, methionine, phenylalanine, tyrosine,
406 and tryptophan) pattern along both directions. Subsequently, these patterns were used
407 to search against the sequences of SWI/SNF subunits on the Sequence pattern search
408 server (<http://www-archbac.u-psud.fr/genomics/patternSearch.html>), and Swi1 942-955
409 was one of the best hit. Further extension of this helix into connected density also
410 matched the secondary structures of Swi1. Then, the remaining regions of the Swi1
411 ARM repeat domain were manually built into the density in Coot based on secondary
412 structure prediction as well as bulky sidechain densities wherever possible. The overall
413 architecture of the ARM repeat domain of Swi1 also matches that of an Armadillo repeat
414 containing protein β -catenin³² (Extended Data Fig. 8a), confirming our model of Swi1.
415
416 The positioning of the SWIB domain of Snf12 aided us in building the remaining of this
417 protein into the density. First, at the Spine tip, where the SWIB was docked, there is β -
418 sheet like density (Extended Data Fig. 6c). This agrees with the secondary structure
419 prediction of Snf12, which shows β -strands right N-terminus of the SWIB domain.

420 Although the resolution of this region is low, we are confident about its identity. Four
421 long helices belonging to the Spine module directly connect to this region, two of which
422 extending into the Snf12 densities. Therefore, we assigned these two helices to Snf12.
423 This agreed well with the secondary structure prediction of Snf12, which shows that
424 Snf12 contains two long helices. Next, we performed protein sequence pattern search
425 based on the bulky sidechain densities. Based on the search results, we manually built
426 the two helices of Snf12 in Coot.

427
428 Based on secondary structure prediction, we reasoned that the other two long helices
429 belong to Swi3 C-terminus. This is backed up by the finding that the C-terminus of Swi3
430 contains a coiled-coil leucine zipper motif²⁶ and there are two copies of Swi3 in
431 SWI/SNF. To facilitate the registering of the sequence in these long helices, we fitted
432 the crystal structure of human OmoMYC homodimer (PDB ID 5I4Z)²⁷ into the density
433 and obtained a good fit (Extended Data Fig. 6a). Based on this fitting, we mapped the
434 hydrophobic residues from Swi3 as indicated before²⁶ and manually built the two helices
435 in Coot. The rest of Swi3 density cannot be confidently modeled due to lower resolution
436 and missing density, therefore are modeled with poly-alanine.

437
438 Snf6 was also manually built in Coot based on secondary structure prediction, bulky
439 sidechain density and prior knowledge based on chemical crosslinking and mass
440 spectrometry data²² and site-directed DNA crosslinking experiments³⁹. We cannot
441 confidently model in Swp82, however we were able to assign densities to this yeast
442 specific subunit based on crosslinking experiments²² and mapping by deletions and

443 EM⁶⁸. The N-terminal region of Swp82 forms a RSC7 homology domain, therefore we
444 speculate that it occupies the globular density near the Hinge; C-terminal region
445 crosslinks to both Snf5 and Swi3, therefore it was assigned to the density by Snf5 and
446 Swi3. There are also several unassigned densities on the solvent exposed surface of
447 the complex. We did not identify Taf14 and Snf11 in the map (Extended Data Table 3).

448
449 The molecular model of SWI/SNF Body module was then refined using Namdinator⁶⁹
450 (Extended Data Table 2). To obtain the model for the full complex, we rigid-body fitted
451 the Body, the Arp module (PDB ID 4I6M)³³ and the ATPase-nucleosome bound with
452 ADP-BeF_x (PDB ID 5Z3V)¹⁵ into the map of the full complexes in Coot. Then, the HSA
453 helix was connected manually, and the DNA sequence was modified to match our
454 sequence. The extra DNA was manually extended by 10bp using B form DNA in Coot.
455 The figures were prepared using UCSF Chimera and ChimeraX⁷⁰. C α -C α distances
456 from crosslinked lysine pairs²² were measured in UCSF Chimera. For crosslinks
457 involving the two molecules of Swi3, we picked the combination that gave the shortest
458 distance as the measurement (Extended Data Table 1).

459

460 **Data availability**

461 Cryo-EM density maps have been deposited in the Electron Microscopy Data Bank
462 (EMDB) under accession numbers EMD-XXXX (ADP-BeF_x), EMD-XXXX (ATP γ S), EMD-
463 XXXX (body). Model coordinates have been deposited in the Protein Data Bank (PDB)
464 under accession numbers XXXX (ADP-BeF_x), XXXX (body).

465

466 **Acknowledgement**

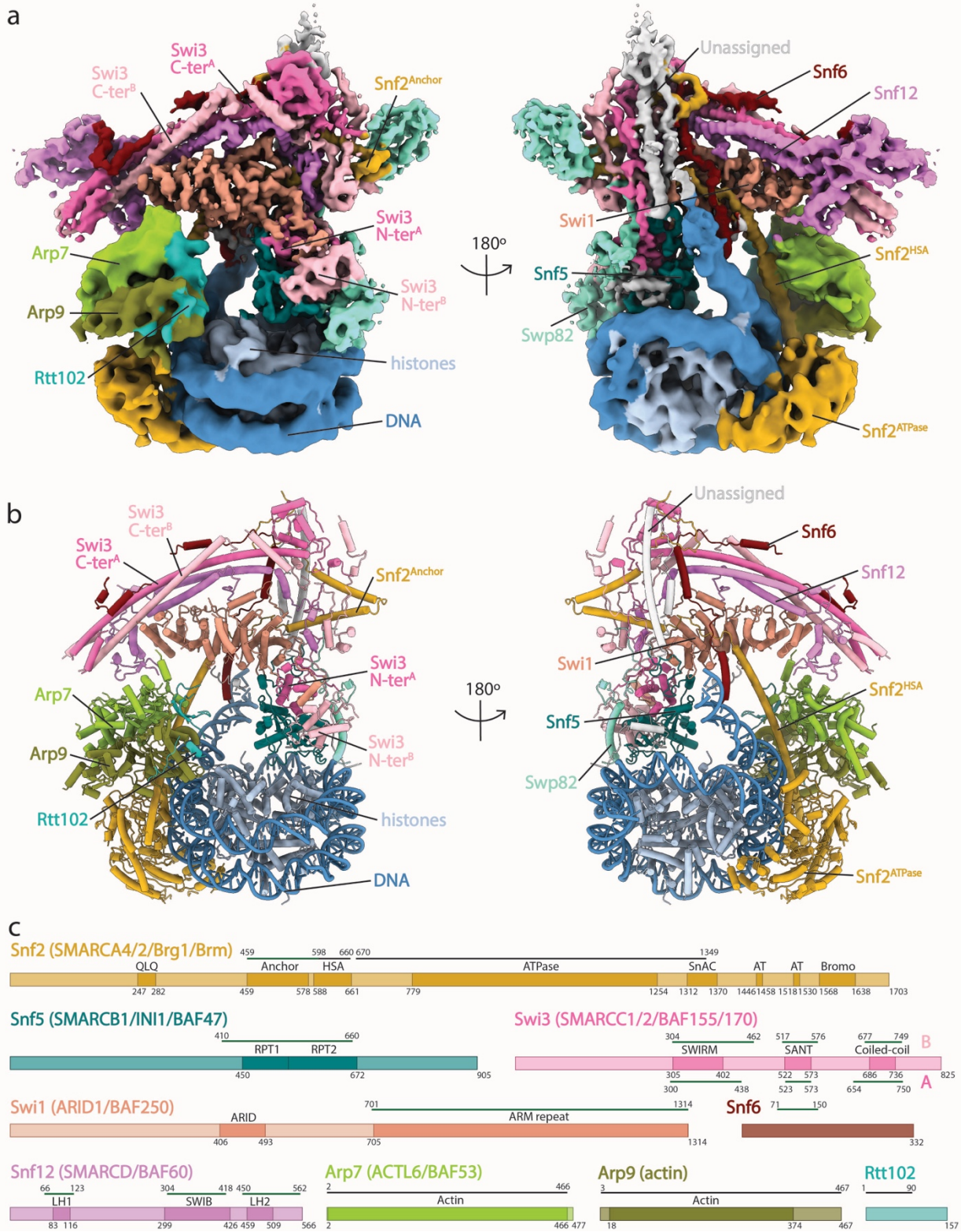
467 We thank Dr. Jonathan Remis for assistance with microscope operation and data
468 collection and Jason Pattie for computer support. We are grateful to Amy Rosenzweig,
469 Ishwar Radhakrishnan and Susan Fishbain for helpful discussion and comments on the
470 manuscript. We also thank the staff at the Structural Biology Facility (SBF) of
471 Northwestern University for technical support. This work was supported by a Cornew
472 Innovation Award from the Chemistry of Life Processes Institute at Northwestern
473 University (to Y He), a Catalyst Award by the Chicago Biomedical Consortium with
474 support from the Searle Funds at The Chicago Community Trust (to Y He), an
475 Institutional Research Grant from the American Cancer Society (IRG-15-173-21 to Y
476 He), an H Foundation Core Facility Pilot Project Award (to Y He). Y He is supported by
477 P01 CA092584 and U54CA193419 from NIH/NCI. Y Han is a recipient of the Chicago
478 Biomedical Consortium Postdoctoral Research Grant.

479

480 **Author contributions**

481 Y Han and Y He conceived the project. Y Han performed most of the experiments and
482 collected and analyzed cryo-EM data with Y He. AA Reyes and S Malik contributed to
483 protein purification. Y Han built the models with help from Y He. Y Han and Y He wrote
484 the manuscript, with input from all other authors.

485 Main Figures



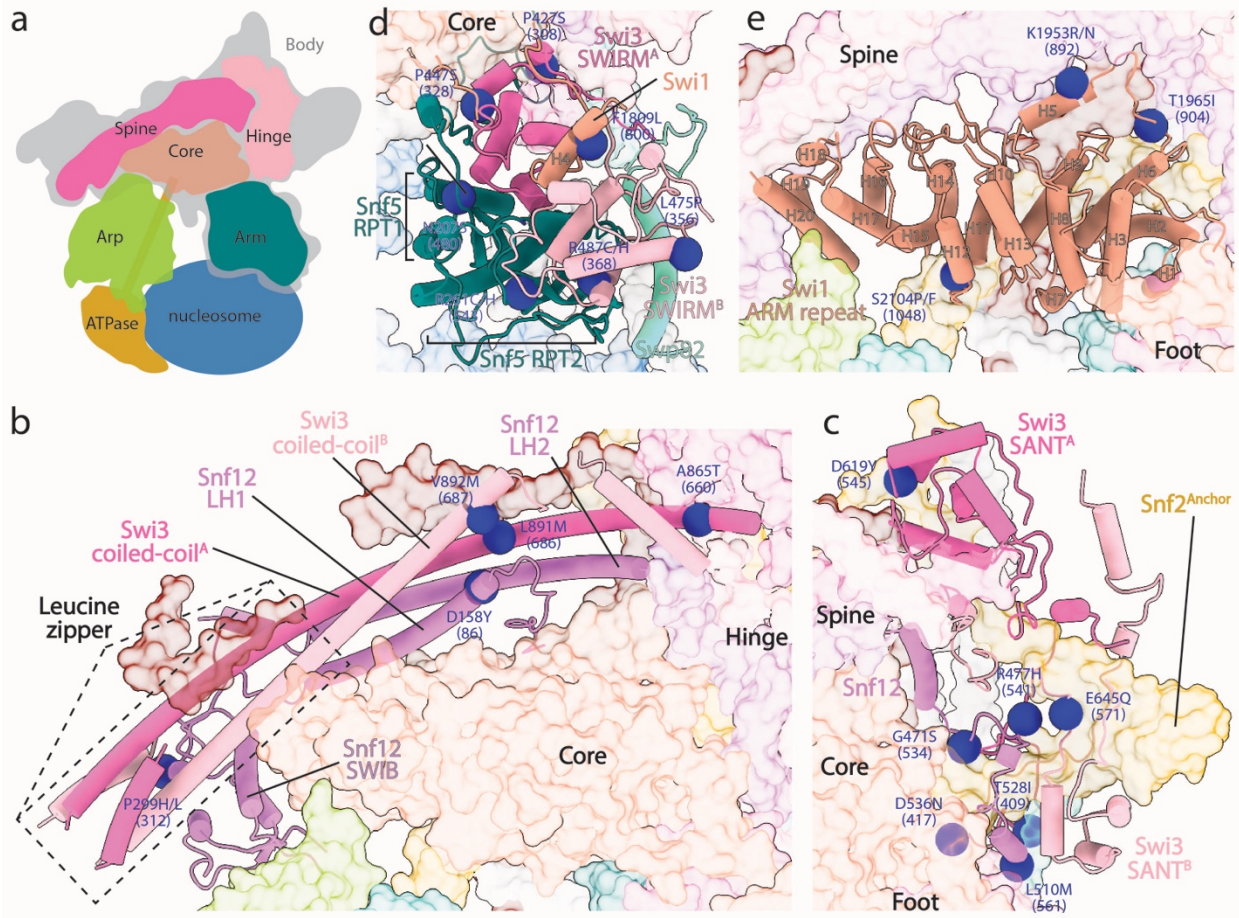
487

488 **Fig. 1: Cryo-EM structure of the SWI/SNF-nucleosome complex.** **a**, Front (left) and
489 back (right) views of the cryo-EM composite map (see Methods) of the SWI/SNF-
490 nucleosome complex assembled in the presence of ADP-BeF_x. **b**, Same views of
491 structural model of the SWI/SNF-nucleosome complex as in **a**. **c**, Domain organization
492 of all subunits that has been built in the model from **b**. Mammalian homologs are shown
493 in parentheses. Newly built or homology regions are highlighted by green lines with
494 residue numbers, whereas previous structures that were rigid body docked in our map
495 are indicated by black lines. Subunits in **b** and **c** are colored as in **a**. Abbreviations:
496 QLQ, Glutamine-Leucine-Glutamine; HSA, Helicase/SANT-associated; SnAC, Snf2
497 ATP coupling; AT, AT hook DNA-binding motif; RPT, Snf5 core repeat; SWIRM, a
498 protein domain found in SWI3, RSC8 and MOIRA; SANT, SWI3, ADA2, N-CoR and
499 TFIIB" DNA-binding; ARID, AT-rich interaction domain; ARM repeat, Armadillo repeat;
500 LH1/2, long helix 1/2; SWIB, SWI complex BAF60b.

501

502

503



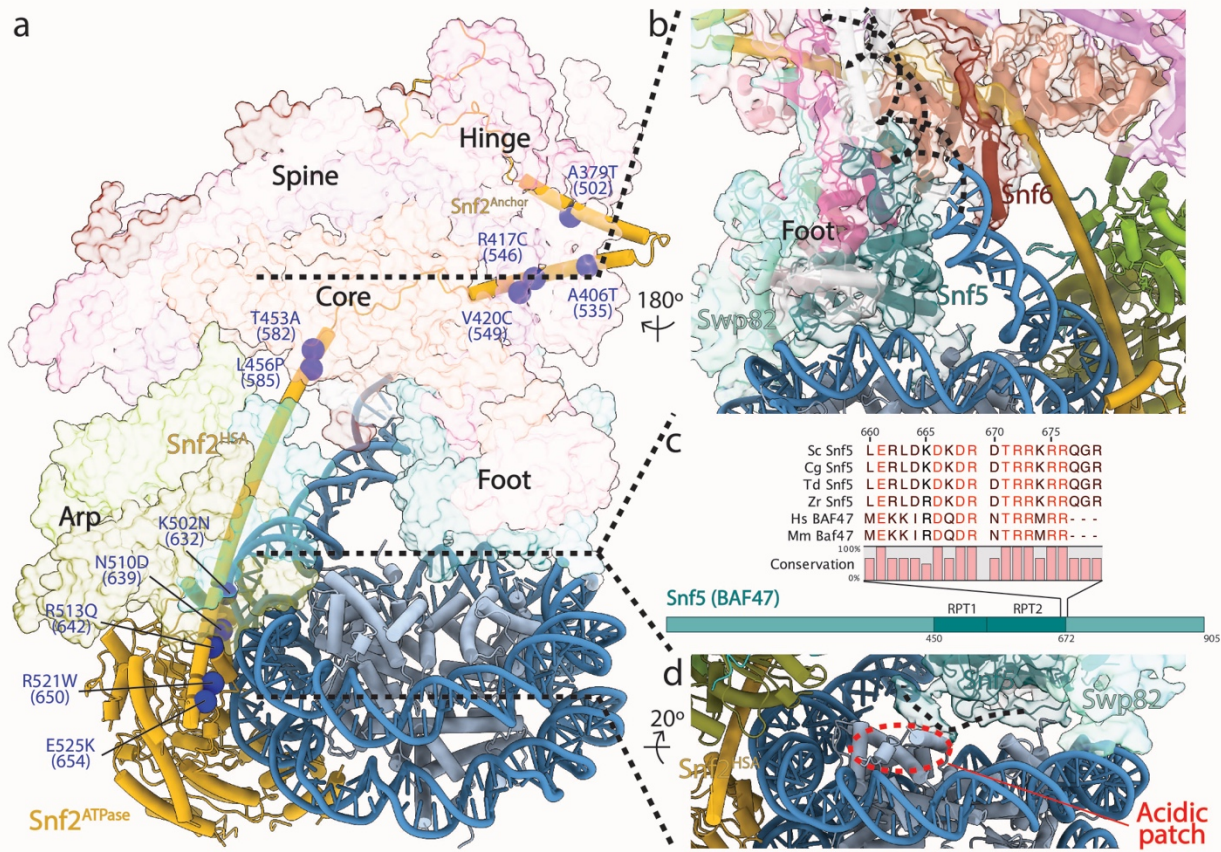
504

505

506 **Fig. 2: Structural organization of the Body module of SWI/SNF.** a, A cartoon
507 depicting the molecular architecture of the SWI/SNF-nucleosome complex. b-e, Close-
508 up view of detailed interactions within the Spine (b), the Hinge (c), the Arm (d) and the
509 Core (e) sub-modules, respectively. Blue spheres depict the locations of a subset of
510 invariant residues harboring cancer patient mutations that occur at interfaces between
511 these conserved subunits. Subunits are colored the same as in Fig. 1.

512

513



514

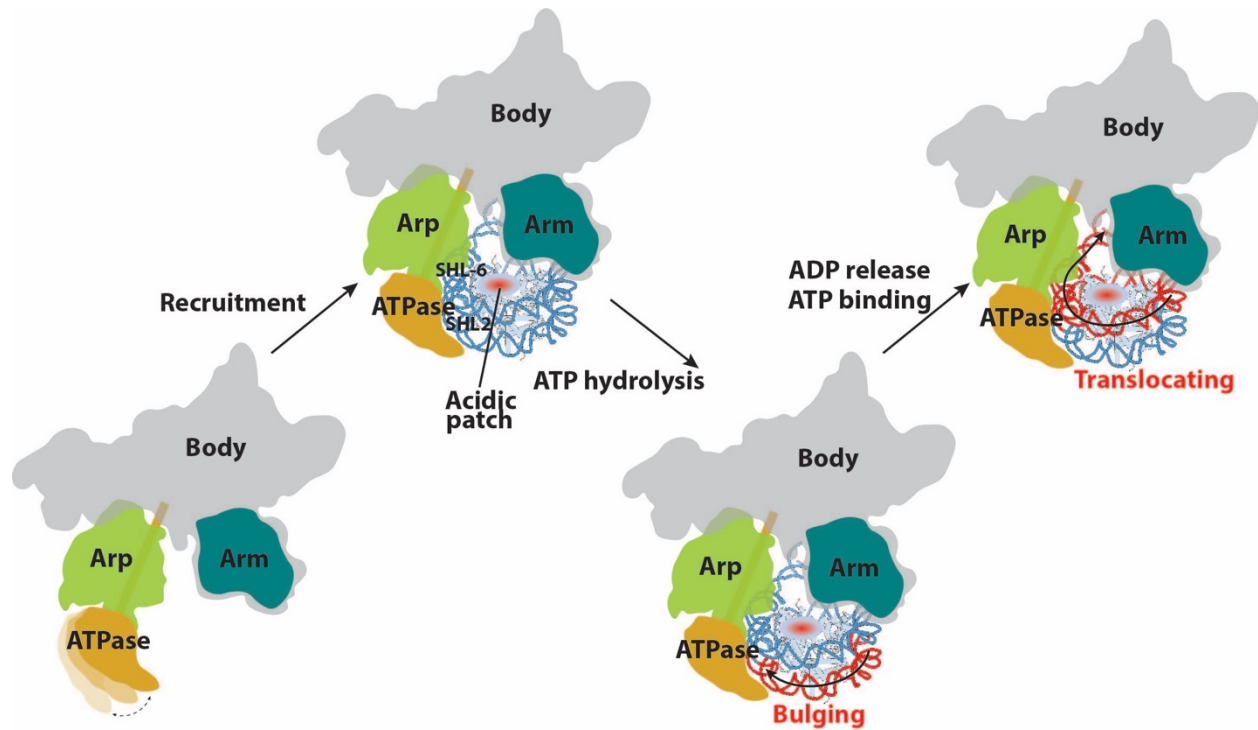
515

516 **Fig. 3: SWI/SNF-nucleosome interactions.** **a**, An overview of the SWI/SNF-
 517 nucleosome complex depicting how the HSA and Anchor domains of Snf2 load the
 518 ATPase onto the nucleosome. Blue spheres indicate the positions of a subset of
 519 invariant residues harboring cancer patient mutations in Snf2/SMARCA4/BRG1 that
 520 reside between conserved SWI/SNF subunits. Dotted lines indicate regions enlarged in
 521 **b** and **d**. **b**, Close-up view showing the interaction between SWI/SNF subunits and the
 522 nucleosomal DNA. **c**, Sequence alignment of the C-terminal extension of Snf5 RPT2.
 523 Sc, *Saccharomyces cerevisiae*; Cg, *Candida glabrata*; Td, *Torulaspora delbrueckii*; Zr,
 524 *Zygosaccharomyces rouxii*; Hs, *Homo sapiens*; Mm, *Mus musculus*. Domain
 525 organization of Snf5/SMARCB1/INI1/BAF47 is also shown as in **Fig. 1c**. **d**, Close-up

526 view showing the C-terminal extension (dotted line) of Snf5 RPT2 contacting the acidic

527 patch of the nucleosome (dotted red circle).

528



529

530 **Fig. 4: Model for chromatin remodeling activity by the SWI/SNF complex.** Prior to

531 engagement with nucleosome, the ATPase module of SWI/SNF is flexible⁶⁸.

532 Nucleosome binding involves the ATPase and the HSA of Snf2 recognizing SHL2 and

533 SHL-6, respectively. The Arm of SWI/SNF interact with the nucleosome surface near

534 the acidic patch, likely serving as an anchor during active remodeling to keep the

535 octamer from moving. Upon ATP hydrolysis, a bulge in the nucleosomal DNA is

536 introduced at SHL 2¹⁵, which is then propagated to the Exit side of the nucleosome

537 when ADP is released and the next ATP molecule is bound, resulting in nucleosomal

538 DNA translocation.

539

540

541 References

- 542 1. Côté, J., Quinn, J., Workman, J. L. & Peterson, C. L. Stimulation of GAL4
543 derivative binding to nucleosomal DNA by the yeast SWI/SNF complex. *Science*
544 **265**, 53–60 (1994).
- 545 2. Cairns, B. R., Kim, Y. J., Sayre, M. H., Laurent, B. C. & Kornberg, R. D. A
546 multisubunit complex containing the SWI1/ADR6, SWI2/SNF2, SWI3, SNF5, and
547 SNF6 gene products isolated from yeast. *Proc. Natl. Acad. Sci. U.S.A.* **91**, 1950–
548 1954 (1994).
- 549 3. Peterson, C. L., Dingwall, A. & Scott, M. P. Five SWI/SNF gene products are
550 components of a large multisubunit complex required for transcriptional
551 enhancement. *Proc. Natl. Acad. Sci. U.S.A.* **91**, 2905–2908 (1994).
- 552 4. Bartholomew, B. Regulating the chromatin landscape: structural and mechanistic
553 perspectives. *Annu. Rev. Biochem.* **83**, 671–696 (2014).
- 554 5. Clapier, C. R. & Cairns, B. R. The biology of chromatin remodeling complexes.
555 *Annu. Rev. Biochem.* **78**, 273–304 (2009).
- 556 6. Cairns, B. R. Chromatin remodeling machines: similar motors, ulterior motives.
557 *Trends in Biochemical Sciences* **23**, 20–25 (1998).
- 558 7. Kingston, R. E., Bunker, C. A. & Imbalzano, A. N. Repression and activation by
559 multiprotein complexes that alter chromatin structure. *Genes & Development* **10**,
560 905–920 (1996).
- 561 8. Peterson, C. L. & Tamkun, J. W. The SWI-SNF complex: a chromatin remodeling
562 machine? *Trends in Biochemical Sciences* **20**, 143–146 (1995).
- 563 9. Vignali, M., Hassan, A. H., Neely, K. E. & Workman, J. L. ATP-dependent
564 chromatin-remodeling complexes. *Molecular and Cellular Biology* **20**, 1899–1910
565 (2000).
- 566 10. Narlikar, G. J., Sundaramoorthy, R. & Owen-Hughes, T. Mechanisms and
567 functions of ATP-dependent chromatin-remodeling enzymes. *Cell* **154**, 490–503
568 (2013).
- 569 11. Rando, O. J. & Winston, F. Chromatin and transcription in yeast. *Genetics* **190**,
570 351–387 (2012).
- 571 12. Rawal, Y. *et al.* SWI/SNF and RSC cooperate to reposition and evict promoter
572 nucleosomes at highly expressed genes in yeast. *Genes & Development* **32**, 695–
573 710 (2018).
- 574 13. Kubik, S. *et al.* Opposing chromatin remodelers control transcription initiation
575 frequency and start site selection. *Nature Structural & Molecular Biology* **26**, 744–
576 754 (2019).
- 577 14. Liu, X., Li, M., Xia, X., Li, X. & Chen, Z. Mechanism of chromatin remodelling
578 revealed by the Snf2-nucleosome structure. *Nature* **544**, 440–445 (2017).
- 579 15. Li, M. *et al.* Mechanism of DNA translocation underlying chromatin remodelling by
580 Snf2. *Nature* **567**, 409–413 (2019).
- 581 16. Willhoft, O. *et al.* Structure and dynamics of the yeast SWR1-nucleosome
582 complex. *Science* **362**, eaat7716 (2018).
- 583 17. Farnung, L., Vos, S. M., Wigge, C. & Cramer, P. Nucleosome-Chd1 structure and
584 implications for chromatin remodelling. *Nature* **550**, 539–542 (2017).

- 585 18. Sundaramoorthy, R. *et al.* Structural reorganization of the chromatin remodeling
586 enzyme Chd1 upon engagement with nucleosomes. *Elife* **6**, 1405 (2017).
- 587 19. Armache, J.-P. *et al.* Cryo-EM structures of remodeler-nucleosome intermediates
588 suggest allosteric control through the nucleosome. *Elife* **8**, 213 (2019).
- 589 20. Eustermann, S. *et al.* Structural basis for ATP-dependent chromatin remodelling
590 by the INO80 complex. *Nature* **556**, 386–390 (2018).
- 591 21. Ayala, R. *et al.* Structure and regulation of the human INO80-nucleosome
592 complex. *Nature* **556**, 391–395 (2018).
- 593 22. Sen, P. *et al.* Loss of Snf5 Induces Formation of an Aberrant SWI/SNF Complex.
594 *Cell Rep* **18**, 2135–2147 (2017).
- 595 23. Merkle, E. D. *et al.* Distance restraints from crosslinking mass spectrometry:
596 mining a molecular dynamics simulation database to evaluate lysine-lysine
597 distances. *Protein Sci.* **23**, 747–759 (2014).
- 598 24. Mashtalir, N. *et al.* Modular Organization and Assembly of SWI/SNF Family
599 Chromatin Remodeling Complexes. *Cell* **175**, 1272–1288.e20 (2018).
- 600 25. Treich, I., Ho, L. & Carlson, M. Direct interaction between Rsc6 and
601 Rsc8/Swh3, two proteins that are conserved in SWI/SNF-related complexes.
602 *Nucleic Acids Research* **26**, 3739–3745 (1998).
- 603 26. Wang, W. *et al.* Diversity and specialization of mammalian SWI/SNF complexes.
604 *Genes & Development* **10**, 2117–2130 (1996).
- 605 27. Jung, L. A. *et al.* OmoMYC blunts promoter invasion by oncogenic MYC to inhibit
606 gene expression characteristic of MYC-dependent tumors. *Oncogene* **36**, 1911–
607 1924 (2017).
- 608 28. Cairns, B. R., Levinson, R. S., Yamamoto, K. R. & Kornberg, R. D. Essential role
609 of Swp73p in the function of yeast Swi/Snf complex. *Genes & Development* **10**,
610 2131–2144 (1996).
- 611 29. Yan, L., Xie, S., Du, Y. & Qian, C. Structural Insights into BAF47 and BAF155
612 Complex Formation. *Journal of Molecular Biology* **429**, 1650–1660 (2017).
- 613 30. Peifer, M., Berg, S. & Reynolds, A. B. A repeating amino acid motif shared by
614 proteins with diverse cellular roles. *Cell* **76**, 789–791 (1994).
- 615 31. Sandhya, S., Maulik, A., Giri, M. & Singh, M. Domain architecture of BAF250a
616 reveals the ARID and ARM-repeat domains with implication in function and
617 assembly of the BAF remodeling complex. *PLoS ONE* **13**, e0205267 (2018).
- 618 32. Huber, A. H., Nelson, W. J. & Weis, W. I. Three-dimensional structure of the
619 armadillo repeat region of beta-catenin. *Cell* **90**, 871–882 (1997).
- 620 33. Schubert, H. L. *et al.* Structure of an actin-related subcomplex of the SWI/SNF
621 chromatin remodeler. *PNAS* **110**, 3345–3350 (2013).
- 622 34. Yang, X., Zaurin, R., Beato, M. & Peterson, C. L. Swi3p controls SWI/SNF
623 assembly and ATP-dependent H2A-H2B displacement. *Nat Struct Mol Biol* **14**,
624 540–547 (2007).
- 625 35. Dutta, A. *et al.* Composition and Function of Mutant Swi/Snf Complexes. *Cell Rep*
626 **18**, 2124–2134 (2017).
- 627 36. Tate, J. G. *et al.* COSMIC: the Catalogue Of Somatic Mutations In Cancer.
628 *Nucleic Acids Research* **47**, D941–D947 (2019).

- 629 37. Zofall, M., Persinger, J., Kassabov, S. R. & Bartholomew, B. Chromatin
630 remodeling by ISW2 and SWI/SNF requires DNA translocation inside the
631 nucleosome. *Nat Struct Mol Biol* **13**, 339–346 (2006).
- 632 38. Saha, A., Wittmeyer, J. & Cairns, B. R. Chromatin remodeling through directional
633 DNA translocation from an internal nucleosomal site. *Nat Struct Mol Biol* **12**, 747–
634 755 (2005).
- 635 39. Dechassa, M. L. *et al.* Architecture of the SWI/SNF-nucleosome complex.
636 *Molecular and Cellular Biology* **28**, 6010–6021 (2008).
- 637 40. Neely, K. E., Hassan, A. H., Brown, C. E., Howe, L. & Workman, J. L.
638 Transcription activator interactions with multiple SWI/SNF subunits. *Molecular and*
639 *Cellular Biology* **22**, 1615–1625 (2002).
- 640 41. Prochasson, P., Neely, K. E., Hassan, A. H., Li, B. & Workman, J. L. Targeting
641 activity is required for SWI/SNF function in vivo and is accomplished through two
642 partially redundant activator-interaction domains. *MOLCEL* **12**, 983–990 (2003).
- 643 42. Mechanism of transcription factor recruitment by acidic activators. *J. Biol. Chem.*
644 **280**, 21779–21784 (2005).
- 645 43. McGinty, R. K. & Tan, S. Recognition of the nucleosome by chromatin factors and
646 enzymes. *Curr. Opin. Struct. Biol.* **37**, 54–61 (2016).
- 647 44. Ghaemmaghami, S. *et al.* Global analysis of protein expression in yeast. *Nature*
648 **425**, 737–741 (2003).
- 649 45. Lowary, P. T. & Widom, J. New DNA sequence rules for high affinity binding to
650 histone octamer and sequence-directed nucleosome positioning. *Journal of*
651 *Molecular Biology* **276**, 19–42 (1998).
- 652 46. Dyer, P. N. *et al.* Reconstitution of nucleosome core particles from recombinant
653 histones and DNA. *Meth. Enzymol.* **375**, 23–44 (2004).
- 654 47. He, Y. *et al.* Near-atomic resolution visualization of human transcription promoter
655 opening. *Nature* **533**, 359–365 (2016).
- 656 48. Knutson, B. A. Structural mechanism of ATP-independent transcription initiation
657 by RNA polymerase I. *Elife* **6**, 753 (2017).
- 658 49. Han, Y., Yan, C., Fishbain, S., Ivanov, I. & He, Y. Structural visualization of RNA
659 polymerase III transcription machineries. *Cell Discov* **4**, 40 (2018).
- 660 50. Suloway, C. *et al.* Automated molecular microscopy: the new Legimon system.
661 *Journal of Structural Biology* **151**, 41–60 (2005).
- 662 51. Lander, G. C. *et al.* Appion: an integrated, database-driven pipeline to facilitate
663 EM image processing. *Journal of Structural Biology* **166**, 95–102 (2009).
- 664 52. Voss, N. R., Yoshioka, C. K., Radermacher, M., Potter, C. S. & Carragher, B.
665 DoG Picker and TiltPicker: software tools to facilitate particle selection in single
666 particle electron microscopy. *Journal of Structural Biology* **166**, 205–213 (2009).
- 667 53. Rohou, A. & Grigorieff, N. CTFFIND4: Fast and accurate defocus estimation from
668 electron micrographs. *Journal of Structural Biology* **192**, 216–221 (2015).
- 669 54. van Heel, M., Harauz, G., Orlova, E. V., Schmidt, R. & Schatz, M. A new
670 generation of the IMAGIC image processing system. *Journal of Structural Biology*
671 **116**, 17–24 (1996).
- 672 55. Tang, G. *et al.* EMAN2: an extensible image processing suite for electron
673 microscopy. *Journal of Structural Biology* **157**, 38–46 (2007).

- 674 56. Punjani, A., Rubinstein, J. L., Fleet, D. J. & Brubaker, M. A. cryoSPARC:
675 algorithms for rapid unsupervised cryo-EM structure determination. *Nature*
676 *Methods* **14**, 290–296 (2017).
- 677 57. Zheng, S. Q. *et al.* MotionCor2: anisotropic correction of beam-induced motion for
678 improved cryo-electron microscopy. *Nature Methods* **14**, 331–332 (2017).
- 679 58. Zhang, K. Gctf: Real-time CTF determination and correction. *Journal of Structural*
680 *Biology* **193**, 1–12 (2016).
- 681 59. Kimanius, D., Forsberg, B. O., Scheres, S. H. & Lindahl, E. Accelerated cryo-EM
682 structure determination with parallelisation using GPUs in RELION-2. *Elife* **5**,
683 e18722 (2016).
- 684 60. Henderson, R. *et al.* Outcome of the first electron microscopy validation task force
685 meeting. in **20**, 205–214 (2012).
- 686 61. Bai, X.-C., Rajendra, E., Yang, G., Shi, Y. & Scheres, S. H. W. Sampling the
687 conformational space of the catalytic subunit of human γ -secretase. *Elife* **4**, 1485
688 (2015).
- 689 62. Nakane, T., Kimanius, D., Lindahl, E. & Scheres, S. H. Characterisation of
690 molecular motions in cryo-EM single-particle data by multi-body refinement in
691 RELION. *Elife* **7**, 1485 (2018).
- 692 63. Kurowski, M. A. & Bujnicki, J. M. GeneSilico protein structure prediction meta-
693 server. *Nucleic Acids Research* **31**, 3305–3307 (2003).
- 694 64. Pettersen, E. F. *et al.* UCSF Chimera--a visualization system for exploratory
695 research and analysis. *J Comput Chem* **25**, 1605–1612 (2004).
- 696 65. Goddard, T. D., Huang, C. C. & Ferrin, T. E. Visualizing density maps with UCSF
697 Chimera. *Journal of Structural Biology* **157**, 281–287 (2007).
- 698 66. Webb, B. & Sali, A. Comparative Protein Structure Modeling Using MODELLER.
699 *Curr Protoc Bioinformatics* **54**, 5.6.1–5.6.37 (2016).
- 700 67. Emsley, P., Lohkamp, B., Scott, W. G. & Cowtan, K. Features and development of
701 Coot. *Acta Crystallogr. D Biol. Crystallogr.* **66**, 486–501 (2010).
- 702 68. Zhang, Z. *et al.* Architecture of SWI/SNF chromatin remodeling complex. *Protein*
703 *& Cell* **15**, 1–5 (2018).
- 704 69. Kidmose, R. T. *et al.* Namdinator - automatic molecular dynamics flexible fitting of
705 structural models into cryo-EM and crystallography experimental maps. *IUCrJ* **6**,
706 526–531 (2019).
- 707 70. Goddard, T. D. *et al.* UCSF ChimeraX: Meeting modern challenges in
708 visualization and analysis. *Protein Sci.* **27**, 14–25 (2018).
- 709